Final version of this paper was published at
Measurement 221, 113547, 2023 https://doi.org/10.1016/j.measurement.2023.113547

Rotating Speed Measurement Using an Optimized Eddy Current Sensor

Mehran Mirzaei and Pavel Ripka
Faculty of Electrical Engineering, Czech Technical University, Prague, 16627, Czech Republic
(mirzameh@fel.cvut.cz)

***Abstract*—This paper presents the rotating speed measurement of solid iron hollow shafts using the optimum design of a rotational eddy current sensor. The rotating speed measurements are performed using the optimized sensor up to ±3000 rpm to evaluate sensitivity enhancement and linearity performance. The sensor is optimized for a shorter axial length and higher sensitivity with a new configuration of the coils. An aluminum shell on a solid shaft is used, which helps to improve the sensitivity and the susceptibility of the sensor to the material properties of solid iron. A 2D analytical method and a 3D time stepping finite element method are considered for the theoretical analysis of the sensor and for an assessment of the effect of this optimization on the performance. The performance of the sensor was verified by measurements. The evaluation of the speed sensor for higher speeds up to ±30000 rpm is performed using the 2D analytical method.**

***Index Terms*—Eddy current, measurement, modeling, optimum design, speed sensor.**

I. INTRODUCTION

Motion control is essential for all moving machinery, for the purposes of efficient performance, maintenance, and protection [1]-[2]. Speed sensing is therefore needed as a critical input for the control system of industrial applications, for example, electric and hybrid vehicles for transportation systems [3]. Electric vehicles include various mechanical and electrical rotating components. There is increasing utilization of high power density electrical machines with cylindrical and disc configurations in electric and hybrid transportation systems [4]-[5].

Permanent magnet machines have achieved incredible power density [4]. However, they require the use of expensive rare-earth magnets, which are exposed to demagnetization at high temperatures. Induction machines, e.g. traction motors, are promising in terms of cost-effective rotor structures and greater reliability at high temperatures [5]-[11]. The power density of induction machines can be increased with improved thermal management of electrical machines [5]. For example, shaft cooling is an efficient approach that uses oil flowing in the hollow shaft [11]-[15]. However, this makes the structure of induction machines more complicated and leaves less space for physical speed measurement systems [16]. Axial airgap induction machines [9]-[10] have even shorter axial lengths in comparison with cylindrical induction machines. A compact speed sensor is therefore essential for electro-mobility applications.

Sensorless speed measurement methods for induction machines have been extensively developed in terms of high accuracy and applicability for different speed ranges [17]-[18]. Sensorless measurement methods are nondestructive, contactless and nonphysical, and - unlike physical speed sensors – they can be installed without needing to overhaul the machine. However, they are susceptible to electrical faults and are expensive, due to the complicated hardware required for signal processing.

Standard optical encoders and resolvers are the most popular physical sensors for speed measurement [19]-[22]. Optical encoders have excellent precision, and variable reluctance resolvers show high reliability in harsh working conditions. However, these sensors are less reliable when they are exposed to high levels of mechanical vibration, because of the salient optical and reluctance components installed on the rotating shaft. In addition, it is practically impossible to install them on hollow shafts through which cooling oil flows.

Innovative approaches were used for the position and speed sensing of rotating shafts in [23]-[30]. A new approach was presented using linear Hall sensors and optimized bread loaf permanent magnets installed on the hollow shaft, which showed high accuracy and high temperature stability [23]. A novel design of a magnetic rotational sensor was shown in [24] with an eccentrically mounted permanent magnet ring. The rotating permanent magnets face balancing problems at high speeds and vibration operation [23]-[24], which affect the accuracy of speed sensing. A contactless speed sensor using a rotating hetropolar permanent magnet cylinder was proposed in [25] for the linear speed measurement of smooth conductive parts. It was only tested for large rotating aluminum disk. The risk of magnet demagnetization and its effect on the accuracy of rotor position detection were neglected in [23]-[25]. A novel direct position control for ultra high-speed measurement is proposed in [26] based on nonintrusive reflective optical sensors, which were later utilized for the speed measurement of a high speed switched reluctance machine [27]. It uses black non-reflective and white reflective marks installed on the rotating shaft. It suffers the same issues as optical encoders concerning high sensitivity to dust and vibrations.

Final version of this paper was published at
Measurement 221, 113547, 2023 https://doi.org/10.1016/j.measurement.2023.113547

A novel approach using linear Hall sensors installed inside the stators of the permanent magnet machines was presented in [28]-[29] to measure the flux density for detection of the rotor position and speed. The same approach is used in [30] for rotor position and speed measurement of a switched reluctance machine. The installation of magnetometers in the stator exposes the sensor to the overheating caused by the winding and core losses. The implementation of this approach in induction machines is more complicated due to the rotor fields.

Utilizing an eddy current is a convenient method for nondestructive testing and measurement [25], [31]-[32]. Modeling the motional component of the eddy current is essential for making accurate and rapid measurements in nondestructive testing [32]-[33]. The rotational and translational speeds of conductive moving objects can be measured by utilizing the motional component of the induced eddy current. Eddy current sensors with cylindrical configurations are appealing options for speed measurements of rotating hollow shafts [16] and [34]-[35]. There are three main problems with existing designs: 1. low sensitivity, 2. susceptibility to the variability of the properties of the shaft material, 3.excessive length, which is incompatible with novel motors. Each of these three problems is addressed in this paper.

A rotational eddy current speed sensor with perpendicular coils for solid iron shafts up to ±3000 rpm was presented in [35]. In this paper the optimized design of a similar sensor intended for a hollow shaft was presented. The new sensor is shorter and more sensitive than the first version, described in [35]. The new design of the sensor presented here features two main innovations: 1. a larger number of excitation coils and pickup coils, and 2. a nonmagnetic conductive shell. A conductive shell was already used for solid rods in [34]. The optimized sensor has a 43.8% shorter axial length than the sensor described in [16], together with 125% higher sensitivity. In addition, these parameters are achieved with an only hollow shaft. Using a thin aluminum shell on the hollow shaft further improves the sensitivity by 500%-600%. The presented sensor has a robust and simple structure, which is a critical feature for high-speed applications with high mechanical vibrations, e.g. for vehicle traction machinery.

II. Structure and Theory of Performance

Fig. 1 shows 3D models of an eddy current speed sensor and hollow shafts. A conductive nonmagnetic shell is used on the hollow shaft in Fig. 1 b). The sensor has two sets of coils, E and P, as excitation and pickup coils. Each set comprises four coils. Each set of coils can be considered as excitation coils or as pickup coils, according to the reciprocity theorem.

Fig. 2 shows the magnetic flux distribution in the sensor and the hollow solid iron shaft at zero speed and at nonzero speed when set of coils E is used as the excitation coils. The magnetic flux distribution is symmetric in Fig. 2 a) when the speed is zero. Therefore, the net flux linkage and the induced voltage are zero in set of coils P as pickup coils. However, the speed of the rotating shaft generates motional eddy currents in the solid shaft, which makes the magnetic flux distribution asymmetric in Fig. 2 b). This causes an induced voltage in the pickup coils with AC excitation, which is proportional to the speed. The induced voltage can be used to measure the rotating speed.

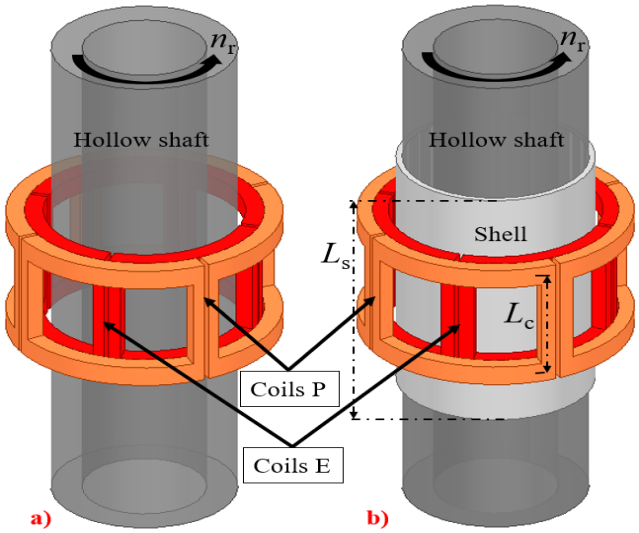

Fig. 1. 3D model of eddy current speed sensors for rotating hollow shafts, a) only iron shaft, b) iron shaft with a shell.

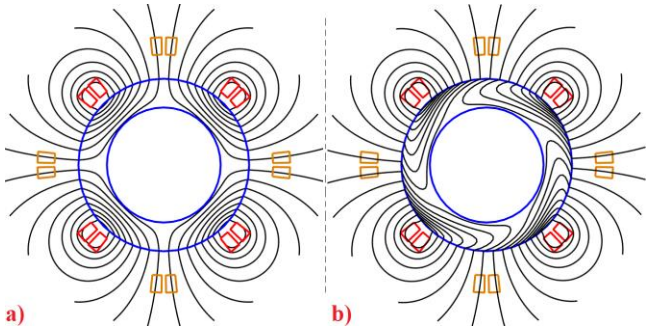

Fig. 2. Magnetic flux distribution in the sensor and the hollow iron shaft, a) at zero speed, b) at nonzero speed.

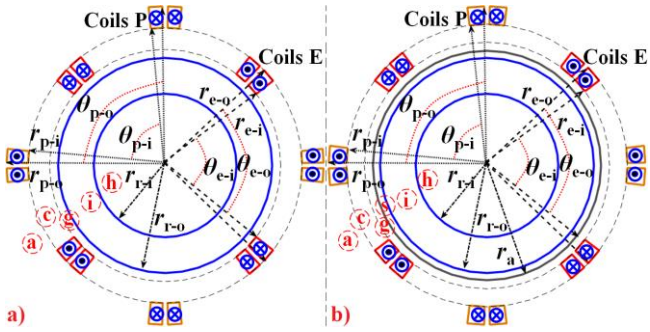

Fig. 3. 2D model of eddy current speed sensors, winding connections and the dimensions, a) only iron shaft with coils A, b) iron shaft and a conductive shell with coils B

III. 2D Analytical Modeling

A 2D computational model of the sensor with winding directions and dimensions is shown in Fig. 3. It is divided into several parts for analytical computation, as shown in Fig. 3 a) and Fig. 3 b). Coils set E is considered for excitation, and coils

Final version of this paper was published at
Measurement 221, 113547, 2023 https://doi.org/10.1016/j.measurement.2023.113547

set P is considered for pickup.
h - is the air region inside the hollow shaft,
i - is the iron region of the hollow shaft,
s - is the conductive shell region on the hollow shaft,
g - is the air gap region between the coils and the hollow shaft in Fig. 3 a), or between the coils and the conductive shell in Fig. 3 b),
c - is the excitation coils region, and
a - is the air region beyond the excitation coils E, including the pickup coils P.

Fig. 3 shows the geometrical parameters of the sensor with coils A for only hollow shafts and the sensor with coils B for a hollow shaft with conductive shells. $r_{r\text{-}i}$, $r_{r\text{-}o}$ and r_a are the inner radius, the outer radius of the hollow shaft, and the outer radius of the aluminum shell, respectively. $r_{e\text{-}i}$, $r_{e\text{-}o}$, $r_{p\text{-}i}$ and $r_{e\text{-}o}$ are the inner radius and the outer radii of the excitation coils, and the inner and outer radii of the pickup coils, respectively. $\theta_{e\text{-}i}$ and $\theta_{e\text{-}o}$ are the inner and outer angles of the excitation coils, and $\theta_{p\text{-}i}$ and $\theta_{p\text{-}o}$ are the inner and outer angles of the pickup coils.

Six differential partial equations for six regions, in cylindrical coordinates, versus the z-component of the magnetic vector potential A_z are presented in (1), extracted from the Maxwell equations [35]-[36]. The number of differential equations is reduced to five when the sensor with only a hollow shaft and with no aluminum shell on the shaft, region s, is analyzed.

$$\begin{gathered}\frac{1}{r}\frac{\partial}{\partial r}\left(r\frac{\partial A_{z,h}}{\partial r}\right)+\frac{1}{r^2}\frac{\partial^2 A_{z,h}}{\partial\theta^2}=0\\ \frac{1}{r}\frac{\partial}{\partial r}\left(r\frac{\partial A_{z,i}}{\partial r}\right)+\frac{1}{r^2}\frac{\partial^2 A_{z,i}}{\partial\theta^2}=\mu_0\mu_r\sigma_i'\left(j\omega A_{z,i}+\omega_r\frac{\partial A_{z,i}}{\partial\theta}\right)\\ \omega=2\pi f\quad,\quad \omega_r=2\pi\frac{n_r}{60}\\ \frac{1}{r}\frac{\partial}{\partial r}\left(r\frac{\partial A_{z,s}}{\partial r}\right)+\frac{1}{r^2}\frac{\partial^2 A_{z,s}}{\partial\theta^2}=\mu_0\sigma_s'\left(j\omega A_{z,s}+\omega_r\frac{\partial A_{z,s}}{\partial\theta}\right)\\ \frac{1}{r}\frac{\partial}{\partial r}\left(r\frac{\partial A_{z,g}}{\partial r}\right)+\frac{1}{r^2}\frac{\partial^2 A_{z,g}}{\partial\theta^2}=0\\ \frac{1}{r}\frac{\partial}{\partial r}\left(r\frac{\partial A_{z,c}}{\partial r}\right)+\frac{1}{r^2}\frac{\partial^2 A_{z,c}}{\partial\theta^2}=-\mu_0\cdot J_s\\ \frac{1}{r}\frac{\partial}{\partial r}\left(r\frac{\partial A_{z,a}}{\partial r}\right)+\frac{1}{r^2}\frac{\partial^2 A_{z,a}}{\partial\theta^2}=0\end{gathered}\tag{1}$$

where, σ_i' and σ_a' are the corrected hollow shaft conductivity and the shell conductivity. n_r is the rotational speed in rpm. f is the frequency. μ_r and J_s are the relative magnetic permeability and the current density in the excitation coils, respectively. J_s can be written in Fourier series format:

$$\begin{gathered}J_s=\sum_{m=\pm1,\pm3,\dots}J_{s,m}\cdot e^{j(\omega t-2m\theta)}\\ J_{s,m}=\frac{2}{jm\pi}(cos(m\theta_{e-i})-cos(m\theta_{e-o}))\cdot\sqrt{2}\frac{N_eI_e}{a_{w,e}}\\ a_{w,e}=\frac{(\theta_{e-o}-\theta_{e-i})}{4}\cdot(r_{e-o}^2-r_{e-i}^2)\end{gathered}\tag{2}$$

where, N_e and I_e are the number of turns per excitation coil and the rms value of the excitation coil current. Parameter m is the harmonic order in the Fourier series.

The 3rd dimension or the transverse edge effect is considered with correction of the iron shaft conductivity σ_i and aluminum shell conductivity σ_a, using coefficients $K_{e\text{-}i}$ and $K_{e\text{-}s}$ [37]:

$$\begin{gathered}\sigma_i'=K_{e-i}\sigma_i\quad,\quad\sigma_s'=K_{e-s}\sigma_s\\ K_{e-i}=1-\frac{\tanh\left(\beta\frac{L_c}{2}\right)}{\beta\frac{L_c}{2}\cdot\left(1+\tanh\left(\beta\frac{L_c}{2}\right)\right)}\\ K_{e-s}=1-\frac{\tanh\left(\beta\frac{L_c}{2}\right)}{\beta\frac{L_c}{2}\cdot\left(1+\tanh\left(\beta\frac{L_c}{2}\right)\tanh\left(\beta\frac{L_s-L_c}{2}\right)\right)}\\ \beta=\frac{\pi}{\tau},\qquad\tau=\frac{2\pi r_{r-o}}{4}\end{gathered}\tag{3}$$

where L_s is the axial length of the conductive shell on the shaft and L_c is the axial length of the straight part of the coil, as shown in Fig. 1.

The method of separation of variables using Fourier series in cylindrical coordinates is used to solve the differential equation in (1). Equations (4), (5), (6), (7), (8) and (9) are the solutions corresponding to regions h, i, s, g, c and a, respectively.

$$A_{z,h}=\sum_{m=\pm1,\pm3,\dots}\left(C_{h-1}r^{|2m|}+C_{h-2}r^{-|2m|}\right)\cdot e^{j(\omega t-2m\theta)}\tag{4}$$

$$\begin{gathered}A_{z,i}=\sum_{m=\pm1,\pm3,\dots}(C_{i-1}I(|2m|,\gamma_i\cdot r)+C_{i-2}K(|2m|,\gamma_i\cdot r))\\ \cdot e^{j(\omega t-2m\theta)}\\ \gamma_i=\sqrt{j\mu_0\mu_r\sigma_i'(\omega-2m\cdot\omega_r)}\end{gathered}\tag{5}$$

$$\begin{gathered}A_{z,s}=\sum_{m=\pm1,\pm3,\dots}(C_{s-1}I(|2m|,\gamma_s\cdot r)+C_{s-2}K(|2m|,\gamma_s\cdot r))\\ \cdot e^{j(\omega t-2m\theta)}\\ \gamma_s=\sqrt{j\mu_0\sigma_s'(\omega-2m\cdot\omega_r)}\end{gathered}\tag{6}$$

$$A_{z,g}=\sum_{m=\pm1,\pm3,\dots}\left(C_{g-1}r^{|2m|}+C_{g-2}r^{-|2m|}\right)\cdot e^{j(\omega t-2m\theta)}\tag{7}$$

$$\begin{gathered}A_{z,c}=\sum_{m=\pm1,\pm3,\dots}\left(C_{c-1}r^{|2m|}+C_{c-2}r^{-|2m|}+A_{c,m}\right)\\ \cdot e^{j(\omega t-2m\theta)}\\ A_{c,m}=\frac{\mu_0J_{s,m}}{4m^2-4}\cdot r^2\,,\qquad|m|\neq1\\ A_{c,m}=\mu_0J_{s,m}\cdot r^2\cdot(1-4\ln(r))\,,\qquad|m|=1\end{gathered}\tag{8}$$

Final version of this paper was published at
Measurement 221, 113547, 2023 https://doi.org/10.1016/j.measurement.2023.113547

$$A_{z,a} = \sum_{m=\pm1,\pm3,\dots} \left(C_{a-1} r^{|2m|} + C_{a-2} r^{-|2m|}\right) \cdot e^{j(\omega t - 2m\theta)} \tag{9}$$

Parameters C_a are constants that are obtained using the boundary conditions in (10) between computational regions. B_r and H_θ are the radial component of the magnetic flux density and the azimuthal component of the magnetic field strength, respectively.

$$\begin{gathered} B_{r,h}(r = 0) = 0 \\ B_{r,h}(r = r_{c-o}) = B_{r,i}(r = r_{c-o}) \\ H_{\theta,h}(r = r_{c-o}) = H_{\theta,i}(r = r_{c-o}) \\ B_{r,i}(r = r_{c-o}) = B_{r,s}(r = r_{c-o}) \\ H_{\theta,i}(r = r_{c-o}) = H_{\theta,s}(r = r_{c-o}) \\ B_{r,s}(r = r_{c-o}) = B_{r,g}(r = r_{c-o}) \\ H_{\theta,s}(r = r_{c-o}) = H_{\theta,g}(r = r_{c-o}) \\ B_{r,g}(r = r_{c-o}) = B_{r,c}(r = r_{c-o}) \\ H_{\theta,g}(r = r_{c-o}) = H_{\theta,c}(r = r_{c-o}) \\ B_{r,c}(r = r_{c-o}) = B_{r,a}(r = r_{c-o}) \\ H_{\theta,c}(r = r_{c-o}) = H_{\theta,a}(r = r_{c-o}) \\ B_{r,a}(r = \infty) = 0 \end{gathered} \tag{10}$$

The induced voltage in the four pickup coils U_p is calculated in (11) using the time derivative of the total flux linkage of the pickup coils Ψ_p. The line integral is performed on the axial length of the pick up coils in the z-direction [16] and [36]. $A^+_{z,a}$ and $A^-_{z,a}$ are the average of the magnetic potential over the cross-section area of each coil side when considering the winding direction to outside-of-plane (+) and inside-plane (-), respectively.

$$\begin{aligned} U_p = -\frac{d\Psi_p}{dt} &= -j\omega 4 N_p \oint A_{z,a} dl \\ &= -j\omega 4 L_c N_p \left(A^+_{z,a} - A^-_{z,a}\right) \end{aligned} \tag{11}$$

Equation (12) for U_p is obtained by performing the integration in (11) using the parameters in (13) and (14). Parameter N_p is the number of turns in each pickup coil.

$$U_p = \frac{j\omega 4 L_c N_p}{a_{w,p}} \sum_{m=\pm1,\pm3,\dots} C_{p,m} \tag{12}$$

$$a_{w,p} = \frac{\left(\theta_{p-o} - \theta_{p-i}\right)}{4} \cdot \left(r^2_{p-o} - r^2_{p-i}\right) \tag{13}$$

$$\begin{gathered} C_{p,m} = C'_{p,m} \frac{1}{m} \left(\cos\left(m\theta_{p-i}\right) - \cos\left(m\theta_{p-o}\right)\right) \cdot e^{jm\frac{\pi}{2}} \\ C'_{p,m} = C_{a-2} \cdot \frac{\left(r_{p-o}^{-|2m|+2} - r_{p-i}^{-|2m|+2}\right)}{-|2m|+2}, \qquad |m| \neq 1 \\ C'_{p,m} = C_{a-2} \cdot \ln\left(\frac{r_{p-o}}{r_{p-i}}\right), \qquad |m| = 1 \end{gathered} \tag{14}$$

TABLE I
EDDY CURRENT SPEED SENSOR PARAMETERS – WITH COILS A AND B

Parameters			Parameters		
$r_{r\text{-}o}$		15 mm	Coils A	$\theta_{e\text{-}i}$	76.0 deg.
$t_i = r_{r\text{-}o} - r_{r\text{-}i}$		2.0, 5.0 mm		$r_{p\text{-}o}$	22.2 mm
r_a		16 mm		$r_{p\text{-}i}$	19.2 mm
N_e		90		$\theta_{p\text{-}o}$	88.0 deg.
N_p		100		$\theta_{p\text{-}i}$	78.0 deg.
L_c		22 mm	Coils B	$r_{e\text{-}o}$	19.7 mm
L_s		50 mm		$r_{e\text{-}i}$	17.2 mm
μ_r		100		$\theta_{e\text{-}o}$	87.7 deg.
σ_i		5.76 MS/m		$\theta_{e\text{-}i}$	74.0 deg.
σ_s		21.3 MS/m		$r_{p\text{-}o}$	22.2 mm
Coils A	$r_{e\text{-}o}$	19.2 mm		$r_{p\text{-}i}$	19.7 mm
	$r_{e\text{-}i}$	16.2 mm		$\theta_{p\text{-}o}$	88.0 deg.
	$\theta_{e\text{-}o}$	87.6 deg.		$\theta_{p\text{-}i}$	75.8 deg.

Table I presents the values of the sensor parameters with coils A for only hollow shafts and with coils B for hollow shafts with a conductive aluminum shell. Two hollow iron shafts are used, with thicknesses of t_i = 2 mm and 5 mm. An aluminum shell with thickness of t_a = 1 mm is used. Linear magnetic modeling with a constant $\mu_r \leq 150$ is considered for the calculation, because the sensor is operated at low fields, and the effects of the magnetic nonlinearity and hysteresis of solid iron can be neglected.

Fig. 4 presents the analytical calculation results of the absolute value (Abs.) of flux linkage Ψ_p and induced voltage U_p to current ratio versus frequency up to 1200 Hz at 3000 rpm. The flux linkage decreases with frequency. The voltage increases with frequency, as it is proportional to the flux linkage multiplied by the frequency. The results with an aluminum shell (Al) are higher due to the higher reaction fields of the induced motional eddy current. This is caused by high conductivity of aluminum shell.

The absolute value of the voltage-to-current ratio U_p/I_e versus the hollow shaft thickness t_i is shown in Fig. 5. This shows that the induced voltage is less dependent on t_i for higher frequencies due to the smaller skin depth. It is also less dependent on t_i with an aluminum shell, which performs as a shield.

Fig. 6 and Fig. 7 present the U_p/I_e ratio versus the electrical and magnetic properties (μ_r and σ_i) of a hollow shaft. U_p/I_e ratios with a 100% increase of μ_r from 75 to 150 are shown in Fig. 6 a) for only hollow shafts, and in Fig. 6 b) for hollow shafts with an aluminum shell. The susceptibility of induced voltage to μ_r is less with an aluminum shell. The same phenomena are valid using an aluminum shell when the U_p/I_e ratio is presented versus the conductivity σ_i of the hollow shafts.

The use of an aluminum shell helps to enhance the sensitivity about 7 to 8 times, and to decrease the susceptibility of the sensor to the material properties of a hollow solid iron shaft.

Final version of this paper was published at
Measurement 221, 113547, 2023 https://doi.org/10.1016/j.measurement.2023.113547

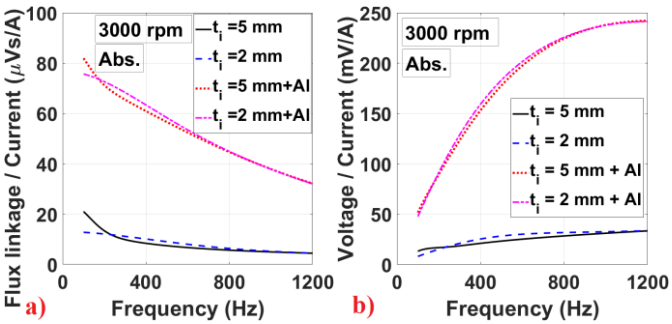

Fig. 4. 2D analytical calculations - a) absolute value (Abs.) of the flux linkage to current ratio versus frequency, b) absolute value of the voltage-to-current ratio versus frequency for hollow shaft thickness t_i = 2 mm and 5 mm with and without an aluminum shell (Al.) – 3000 rpm

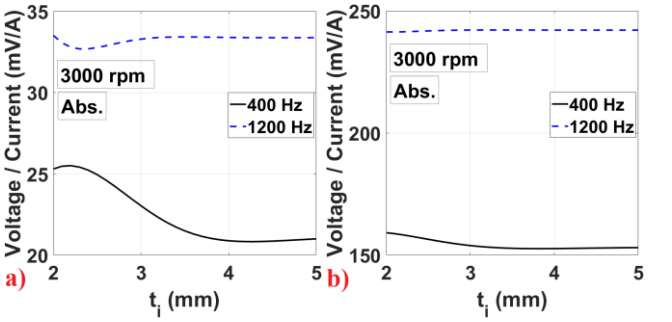

Fig. 5. 2D analytical calculations - absolute value (Abs.) of the voltage-to-current ratio versus the hollow shaft thickness, t_i, a) only iron shaft, b) iron shaft with an aluminum shell – 3000 rpm

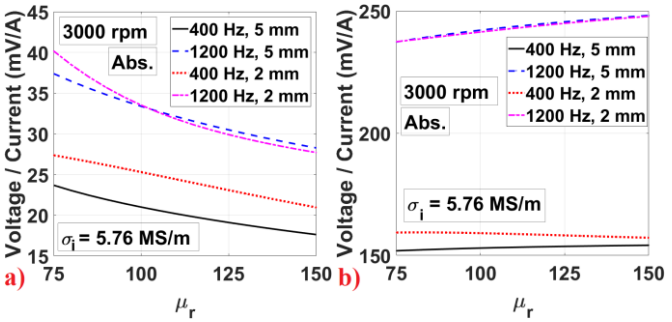

Fig. 6. 2D analytical calculations - absolute value (Abs.) of the voltage-to-current ratio versus shaft relative magnetic permeability, μ_r for hollow shaft thickness t_i = 2 mm and 5 mm, a) only iron shaft, b) iron shaft with an aluminum shell – σ_i = 5.76 MS/m and 3000 rpm

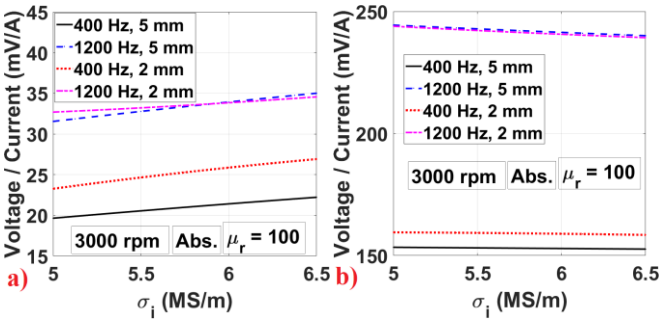

Fig. 7. 2D analytical calculations - absolute value (Abs.) of the voltage-to-current ratio versus shaft conductivity σ_i for hollow shaft thickness t_i = 2 mm and 5 mm, a) only iron shaft, b) iron shaft with an aluminum shell – for μ_r = 100 and 3000 rpm

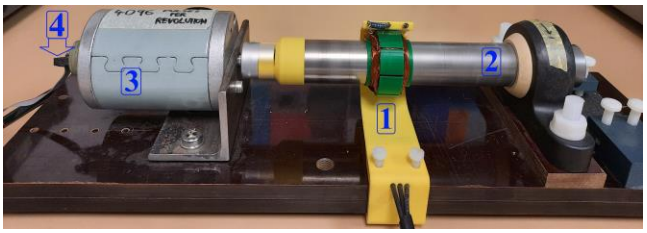

Fig. 8. The experimental setup: 1-sensor, 2- rotation shaft, 3- DC motor as prime mover and 4- GMR sensor

III. Experiments

Fig. 8 shows the experimental setup for the speed measurements of the rotating hollow iron shafts. The hollow shafts are rotated using a controlled DC motor as a prime mover. The measured speed is ±3000 rpm. A TLE5012 absolute angle sensor from Infineon Technologies, based on a giant magnetoresistive (GMR) effect, is used to measure the reference speed [35] shown in Fig. 8. A resolution of 0.01° is achievable using a GMR sensor with a maximum 1.0° angle error. It utilizes the magnetic field of a permanent magnet, which is mounted on the non-drive end shaft of the prime mover. The measurements are performed at two sensor excitation frequencies of 400 Hz and 1200 Hz.

The excitation coils are connected in series, with a total resistance of 23 Ω, and are supplied by a signal generator with an internal resistance of 50 Ω. Additionally, an external resistance of 5.5 Ω in series with the excitation coils is used to measure the current of the excitation coils. The series-connected pickup coils are connected to a lock-in amplifier, Stanford Research System, model SR830 DSP. The lock-in amplifier is used for the measurements of the real U_r and imaginary U_i components of the induced voltages of the pick-up coils, when the current of the excitation coils is considered as a reference signal. The real component of the voltage is in-phase with the excitation coil current, and the imaginary component of the voltage is out-of-phase with the excitation coil current.

Table II presents the rms values of the measured currents at 400 Hz and 1200 Hz for a solid iron hollow shaft with and without the aluminum shell.

TABLE II
Current of Excitation Coils – RMS Value

Material	400 Hz	1200 Hz
Iron, 2 mm	89.9 mA	87.9 mA
Iron, 5 mm	89.9 mA	87.8 mA
Iron, 2 mm + Al	88.8 mA	85.5 mA
Iron, 5 mm + Al	88.8 mA	85.5 mA

A. Results

The measured real and imaginary components of the sensor voltage-to-current ratio U_r/I_e and U_i/I_e versus speed are presented in Fig. 9 and Fig. 10. High linearity of sensor voltage versus speed can be observed. The difference between the sensor voltages for hollow shaft thickness (t_i = 2 mm and t_i = 5 mm) decreases when an aluminum shell with thickness of t_a = 1 mm is used. In our case, the main reason for the difference

Final version of this paper was published at
Measurement 221, 113547, 2023 https://doi.org/10.1016/j.measurement.2023.113547

between the measured voltages for only hollow shafts with t_i = 2 mm and t_i = 5 mm is the different μ_r. The magnetic properties of soft solid iron are highly dependent on the manufacturing process. The effect of the μ_r of the solid iron shaft on the sensor performance can be compensated by using conductive nonmagnetic shells, for example, aluminum, brass, and copper.

The sensitivities K_r, K_i and K_a are calculated using (15), and are presented in Tables III and IV. They are calculated using linear curve fitting functions $U_{r\text{-}c}$, $U_{i\text{-}c}$ and $U_{a\text{-}c}$ to the corresponding real, imaginary, and absolute values of the voltages. K_a increases 5.5 to 7 times when an aluminum shell is used. A second advantage of the non-magnetic shell is almost zero dependence on the thickness of the hollow shaft and μ_r, for example at 1200 Hz.

$$U_{r-c} = K_r \cdot I_e \cdot n_r \quad , \quad U_{i-c} = K_i \cdot I_e \cdot n_r$$
$$U_{a-c} = K_a \cdot I_e \cdot n_r \quad , \quad U_{a-c} = \sqrt{U_{r-c}^2 + U_{i-c}^2} \tag{15}$$

TABLE III
SENSITIVITY OF THE SENSOR – REAL AND IMAGINARY VALUES

	K_r, μV/(A·rpm)		K_i, μV/(A·rpm)	
	400 Hz	1200 Hz	400 Hz	1200 Hz
Iron, 2 mm	6.3	9.0	6.0	8.8
Iron, 5 mm	5.8	9.6	5.7	9.2
Iron, 2 mm + Al	44.3	74.0	35.4	-14.7
Iron, 5 mm + Al	44.0	73.9	35.5	-15.2

TABLE IV
SENSITIVITY OF THE SENSOR – ABSOLUTE VALUE

K_a, μV/(A·rpm)	Iron, 2 mm	Iron, 5 mm	Iron, 2 mm +Al	Iron, 5 mm +Al
400 Hz	8.67	8.16	56.72	56.55
1200 Hz	12.58	13.31	75.45	75.45

The resolution of the eddy current speed sensor depends on the signal processing unit for the sensor voltage. The resolution of 0.25 rpm is achievable for the results in Fig. 9 and Fig. 10 which were measured using SR830 DSP lock-in based on 16-bit Analog-to Digital Converter

B. Nonlinearity Error Analysis

The linearity of the eddy current sensor is evaluated using (16):

$$E_r(\%) = \frac{U_r - U_{r-c}}{U_r(\pm 3000\ \text{rpm})} \times 100$$
$$E_i(\%) = \frac{U_i - U_{i-c}}{U_i(\pm 3000\ \text{rpm})} \times 100 \tag{16}$$

The calculated nonlinearity errors are shown in Fig. 11 and Fig. 12 for real (Re) and imaginary (Im) components of the voltage with maximum values below 1.0%. However, the error can be as low as 0.1%, as shown for the real component of the voltage in Fig. 11 b) at 400 Hz and Fig. 12 b) at 1200 Hz.

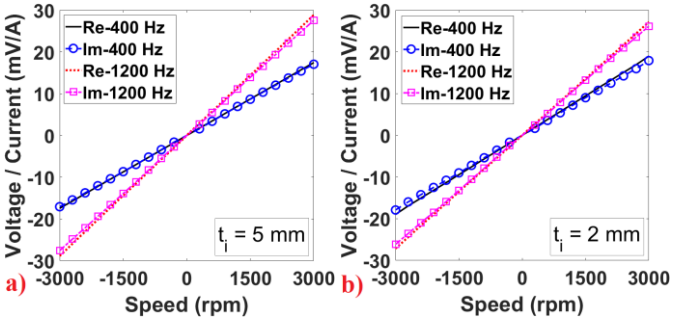

Fig. 9. Measured real (Re) and imaginary (Im) components of the voltage-to-current ratio versus speed up to ±3000 rpm for an only iron shaft, a) for hollow shaft thickness t_i = 5 mm, b) t_i = 2 mm and for excitation frequency of 400 Hz and 1200 Hz

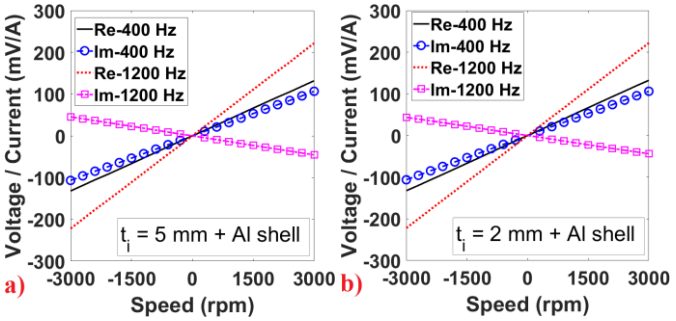

Fig. 10. Measured real (Re) and imaginary (Im) components of the voltage-to-an current ratio versus speed up to ±3000 rpm for an iron shaft with an aluminum shell (Al), a) for hollow shaft thickness t_i = 5 mm, b) t_i = 2 mm – 400 Hz and 1200 Hz

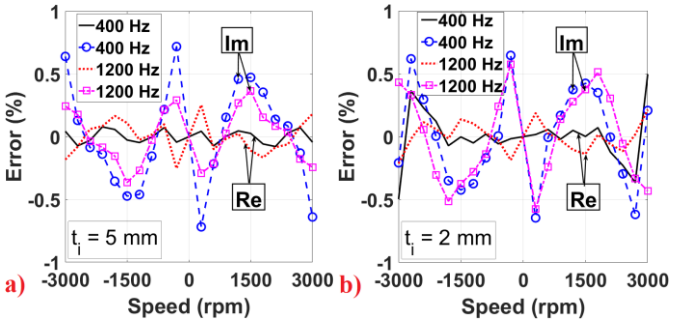

Fig. 11. Calculated nonlinearity error for real (Re) and imaginary (Im) components of the measured voltage-to-current ratio versus speed up to ±3000 rpm for an only iron shaft, a) for hollow shaft thickness t_i = 5 mm, b) for t_i = 2 mm – 400 Hz and 1200 Hz

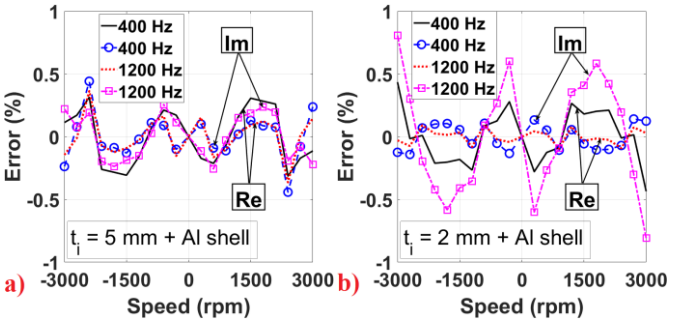

Fig. 12. Calculated nonlinearity error for real (Re) and imaginary (Im) components of the measured voltage-to-current ratio versus speed up to ±3000 rpm for an iron shaft with an aluminum shell, a) for hollow shaft thickness t_i = 5 mm, b) for t_i = 2 mm – 400 Hz and 1200 Hz

Final version of this paper was published at
Measurement 221, 113547, 2023 https://doi.org/10.1016/j.measurement.2023.113547

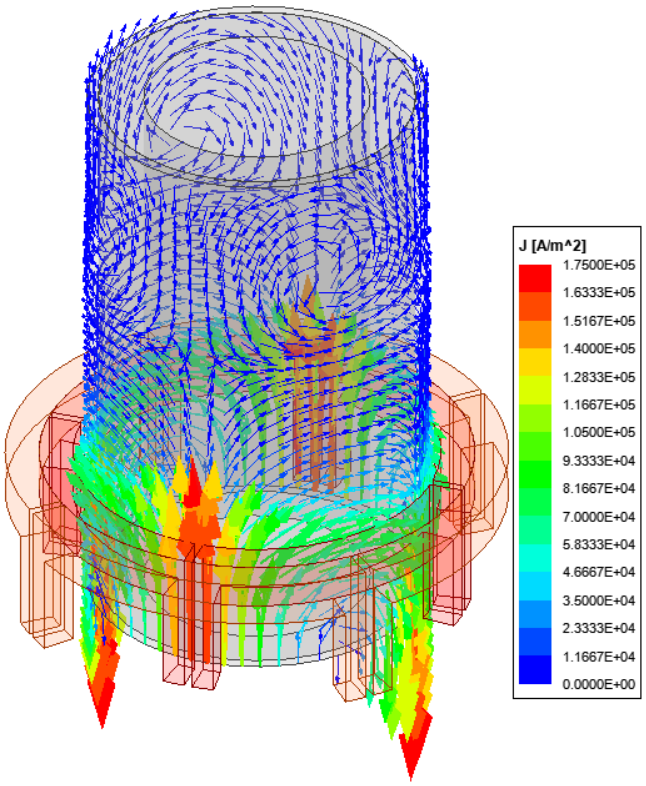

Fig. 13. Eddy current distribution on the rotating shaft using 3D FEM for an only iron shaft, t_i = 5 mm – $\sqrt{2}$ I_e = 15 mA, 3000 rpm, 400 Hz, μ_r = 100 and σ_i = 5.76 MS/m

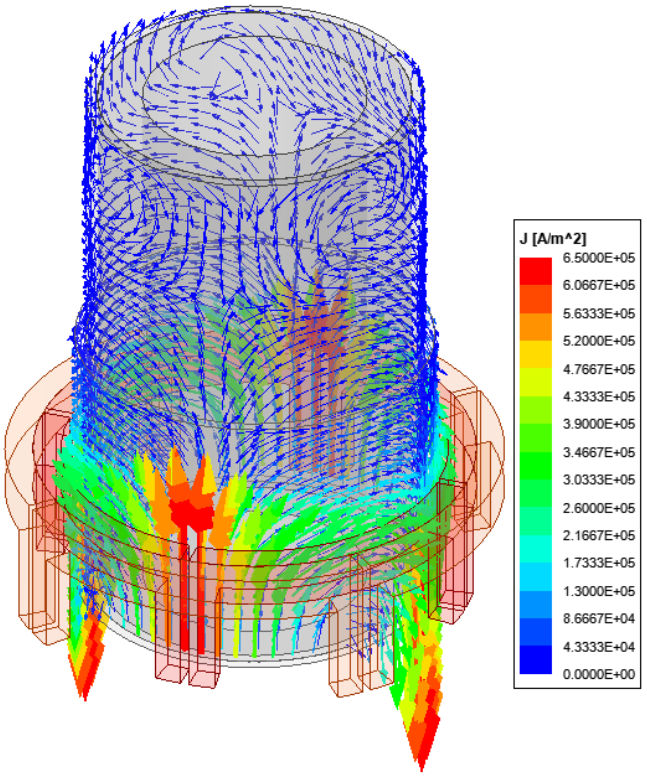

Fig. 14. Eddy current distribution on the rotating shaft using 3D FEM for an iron shaft with aluminum shell, t_i = 5 mm – $\sqrt{2}$ I_e = 15 mA, 3000 rpm, 400 Hz, μ_r = 100 and σ_i = 5.76 MS/m

IV. A Comparison of the Experimental Results and between 3D FEM and the 2D Analytical Methods

3D time stepping FEM is used for precise analysis of the speed sensor, taking directly into account 3D eddy current distribution and shaft rotational speed using ANSYS/Maxwell software. Fig. 13 and Fig. 14 show eddy current distribution at 400 Hz and 3000 rpm for an iron shaft only and an iron shaft with an aluminum shell, respectively. The eddy currents are stronger in the sensor with the shell because of the higher aluminum conductivity. Only half of the model in the axial direction is considered in the 3D FEM simulation because of the symmetry condition.

Table V presents a comparison between the experimental results with 3D time stepping FEM and 2D analytical method calculations at 400 Hz. The results in Table V and VI for only hollow shafts show that decreasing μ_r and increasing σ_i raise the sensitivity. The comparison between the 3D FEM results and the experimental results in Table V for a hollow shaft with an aluminum shell presents an excellent match for different μ_r. This shows the high accuracy of 3D FEM. 3D FEM can therefore be used for further design optimization of the eddy current speed sensor.

TABLE V
Comparison between 3D FEM, the 2D Analytical Method and Experimental Results for Evaluating the Permeability Effect– the Absolute Voltage-to-Current Ratio

3000 rpm, 400 Hz		3D FEM	2D Ana.	Exp.
Iron, t = 2.0 mm	μ_r=75	29 mV/A	27 mV/A	
	μ_r=100	26 mV/A	25 mV/A	26.0
σ_i = 5.76 MS/m	μ_r=150	20 mV/A	21 mV/A	mV/A
Iron, t = 5.0 mm	μ_r=75	22 mV/A	24 mV/A	
	μ_r=100	19 mV/A	21 mV/A	24.5
σ_i = 5.76 MS/m	μ_r=150	16 mV/A	18 mV/A	mV/A
Iron, t = 2.0 mm	μ_r=75	170mV/A	161 mV/A	
+ Al	μ_r=100	169 mV/A	161 mV/A	170.2m
σ_i = 5.76 MS/m	μ_r=150	168mV/A	159 mV/A	V/A
Iron, t = 5.0 mm	μ_r=75	168mV/A	154 mV/A	
+ Al	μ_r=100	170mV/A	155 mV/A	169.7
σ_i = 5.76 MS/m	μ_r=150	171mV/A	156 mV/A	mV/A

TABLE VI
Comparison between 3D FEM, the2D Analytical Method Evaluating the Conductivity Effect – the Absolute Voltage-to-Current Ratio

3000 rpm, 400 Hz		3D FEM	2D Ana.
Iron, t = 2.0 mm	σ_i = 5.0 MS/m	25 mV/A	23 mV/A
μ_r=100	σ_i = 5.76 MS/m	26 mV/A	25 mV/A
	σ_i = 6.5 MS/m	27 mV/A	27 mV/A
Iron, t = 5.0 mm	σ_i = 5.0 MS/m	18 mV/A	20 mV/A
μ_r=100	σ_i = 5.76 MS/m	19 mV/A	21 mV/A
	σ_i = 6.5 MS/m	20 mV/A	22 mV/A
Iron, t = 2.0 mm	σ_i = 5.0 MS/m	171 mV/A	161 mV/A
+ Al	σ_i = 5.76 MS/m	169 mV/A	161 mV/A
μ_r=100	σ_i = 6.5 MS/m	167 mV/A	160 mV/A
Iron, t = 5.0 mm	σ_i = 5.0 MS/m	171 mV/A	155 mV/A
+ Al	σ_i = 5.76 MS/m	170 mV/A	155 mV/A
μ_r=100	σ_i = 6.5 MS/m	169 mV/A	154 mV/A

The 2D analytical method also provides appropriate accuracy in comparison with 3D FEM and in comparison with the experimental results in Tables V and VI and in Fig. 15 and Fig.

Final version of this paper was published at
Measurement 221, 113547, 2023 https://doi.org/10.1016/j.measurement.2023.113547

16. The 2D analytical method is much faster, more cost-effective and easier to use than 3D time stepping FEM using commercial software.

V. Operations at High Speeds

The performance of the sensor is simulated up to ±30000 rpm using the 2D analytical method in order to evaluate the operation of the sensor in a higher speed range. The excitation frequencies are chosen at 4 kHz and 12 kHz to obtain high linearity for high speed ranges, as shown in Fig. 17. The calculated sensitivities corresponding to the absolute voltage value are presented in Table VII. The thickness of the aluminum shell is reduced to t_a = 0.2 mm in Fig. 17 b) to reduce the skin effect at higher excitation frequencies. The sensitivity is lower at 12 kHz for hollow shafts with an aluminum shell in comparison with the sensitivity at 4 kHz, due to the skin effect in the aluminum shell.

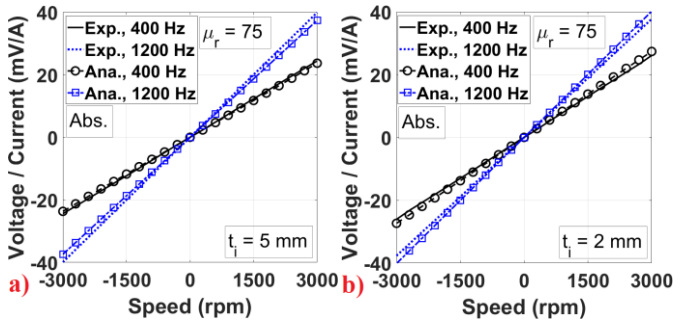

Fig. 15. Comparison between the absolute value of the experimental measured (Exp.) and the 2D analytical calculated (Ana.) voltage-to-current ratio versus speed up to ±3000 rpm for an only iron shaft, a) for a hollow shaft, thickness t_i = 5 mm, b) t_i = 2 mm – 400 Hz and 1200 Hz, μ_r = 75

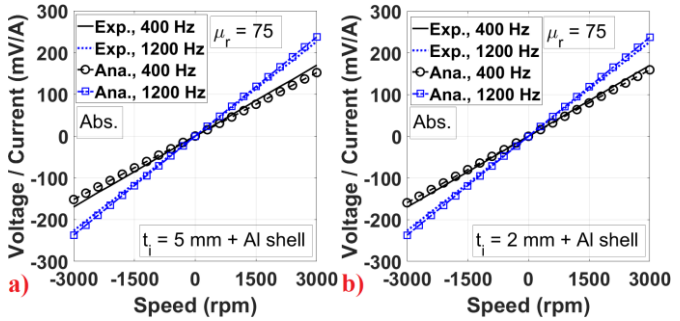

Fig. 16. Comparison between the absolute value of the experimental measured (Exp.) and the 2D analytical calculated (Ana.) voltage-to-current ratio versus speed up to ±3000 rpm for an iron shaft with an aluminum shell, for a hollow shaft thickness a) t_i = 5 mm, b) t_i = 2 mm – 400 Hz and 1200 Hz, μ_r = 75

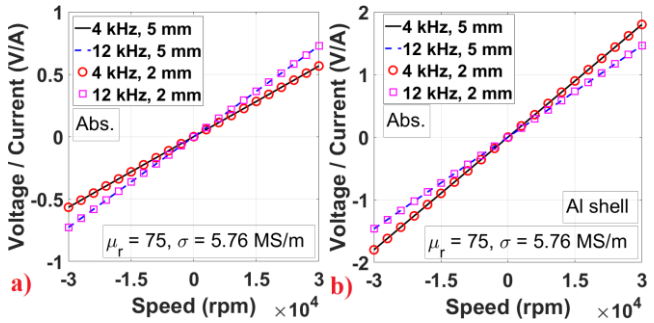

Fig. 17. 2D analytical calculations - absolute value (Abs.) of the voltage-to-current ratio versus speed up to ±30000 rpm for a hollow shaft, thickness t_i = 2 mm and 5 mm, a) an only iron shaft, b) an iron shaft with an aluminum shell – μ_r = 75 and σ_i = 5.76 MS/m

TABLE VII
Sensitivity of the Sensor – Absolute Value (2D Analytical)

K_a, μV/(A·rpm)	Iron, 2 mm	Iron, 5 mm	Iron, 2 mm + Al	Iron, 5 mm + Al
f=4 kHz	18.84	18.84	59.90	59.87
f=12 kHz	24.24	24.24	48.73	48.73

The eddy current and inductive sensors using only excitation and pickup coils have the advantages of a simple, small and robust structure [38]-[39] for the rotating speed measurements.

VI. Topological Optimization of The Speed Sensor

The parameters for the inner and outer angles of the coils, $\theta_{e\text{-}i}$, $\theta_{e\text{-}o}$, $\theta_{p\text{-}i}$, and $\theta_{p\text{-}o}$ are calculated to obtain the required sensitivity of the eddy current speed sensor. Their calculations are performed with consideration of the space constraints and manufacturing complexity to accommodate the excitation and pickup coils. A modified model of an eddy current speed sensor is proposed with thinner coils with the dimensions mentioned in Table VIII. Fig. 18 shows the original and modified models of eddy current speed sensors. The coils dimensions are changed to half radial thickness and the same cross sectional area in comparison with the original model. The results of the original model and the modified model of the eddy current speed sensor are compared in Fig. 19. It is shown that the sensitivity increases by 28.8% for an only iron shaft and by 20.7% for an iron shaft with an aluminum shell. This is caused by thinner coils and a shorter distance between coils centers and the rotating shaft. Therefore, the pickup coils in the modified model have higher flux linkages and induced voltages. However, the manufacturing of thinner coils is more cumbersome.

TABLE VIII
Modified Eddy Current Speed Sensor Parameters – with Coils A and B

Parameters			Parameters		
Coils A	$r_{e\text{-}o}$	17.7 mm	Coils B	$r_{e\text{-}o}$	18.45 mm
	$r_{e\text{-}i}$	16.2 mm		$r_{e\text{-}i}$	17.2 mm
	$\theta_{e\text{-}o}$	87.6 deg.		$\theta_{e\text{-}o}$	87.7 deg.
	$\theta_{e\text{-}i}$	63.4 deg.		$\theta_{e\text{-}i}$	59.40 deg.
	$r_{p\text{-}o}$	19.2 mm		$r_{p\text{-}o}$	19.7 mm
	$r_{p\text{-}i}$	17.7 mm		$r_{p\text{-}i}$	18.45 mm
	$\theta_{p\text{-}o}$	88.0 deg.		$\theta_{p\text{-}o}$	88.0 deg.
	$\theta_{p\text{-}i}$	65.6 deg.		$\theta_{p\text{-}i}$	61.1 deg.

Final version of this paper was published at
Measurement 221, 113547, 2023 https://doi.org/10.1016/j.measurement.2023.113547

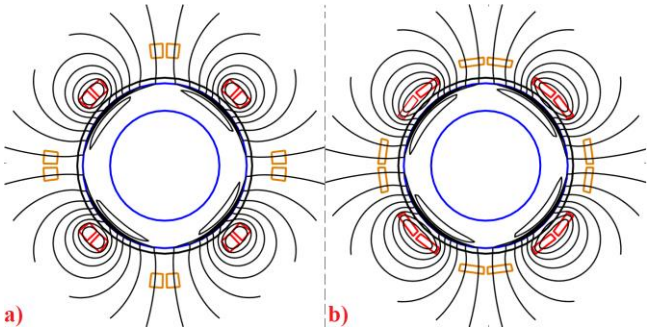

Fig. 18. Magnetic flux distribution, a) original model with dimensions mentioned in Table I, b) modified model to optimize the sensor performance with dimensions mentioned in Table VIII

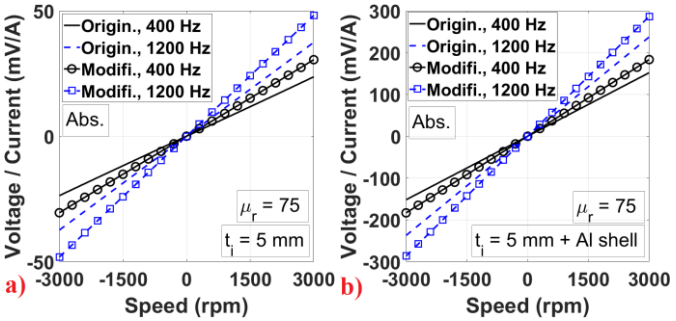

Fig. 19. 2D analytical calculations – The comparison of original and modified models in Fig. 17 for absolute value (Abs.) of the voltage-to-current ratio versus speed up to ±30000 rpm with a hollow shaft, thickness t_i = 5 mm, a) an only iron shaft, b) an iron shaft with an aluminum shell – μ_r = 75 and σ_i = 5.76 MS/m

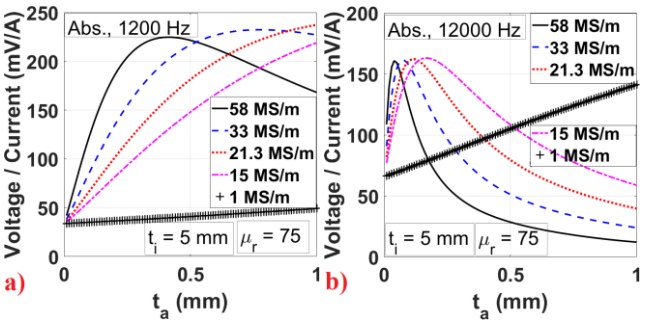

Fig. 20. 2D analytical calculations - absolute value (Abs.) of the voltage-to-current ratio versus the shell thickness, t_a for various nonmagnetic materials a) 1200 Hz, b) 12000 kHz – 3000 rpm

The conductivity, σ_A and thickness, t_A of the nonmagnetic shell have a high influence on the sensitivity of the eddy current speed sensor, as shown at 1200 Hz in Fig. 20 a) and 12000 Hz in Fig. 20 b). The materials of copper, σ_A = 58 MS/m, aluminum, σ_A = 33.0 and 21.3 MS/m, brass, σ_A = 15 MS/m and stainless steel, σ_A = 1.0 MS/m are considered for the simulations. The sensitivity is maximum for a thinner shell with higher conductivity at higher frequencies due to the bigger flux penetration. It is the opposite for stainless steel, as it has much lower conductivity. Using thin aluminum or copper tapes is feasible for thin shells. For example, copper tape with a thickness of 70 µm was used in the rotational eddy current speed sensor [34]. Copper or aluminum electroplating is also feasible when a thin shell thickness is required at high frequencies for high speed operation.

VII. Dynamic Analysis

Dynamic modeling of an eddy current speed sensor is evaluated using 2D time stepping FEM. Eccentricity, run-out, and acceleration effects on the eddy current speed sensor performance are considered. Run-out, shaft gesture, and eccentricities occur when a mechanical inaccuracy exists in the rotating machines. This causes the rotating part to not align with the main axis of the rotating machine. Static and dynamic eccentricities are caused by mechanical manufacturing errors. The eccentricity is modeled as shown in Fig. 21 using 2D time stepping FEM analysis. For example, a 0.6 mm eccentricity is applied, which is 50% of the mechanical gap between coils and the rotating part, g_m = 1.2 mm. It merely shows 0.38% deviation for an only iron shaft and about 0.1% deviation for an iron shaft with an aluminum shell at 1200 Hz and 3000 rpm. Therefore, run-out and eccentricity effects on the accuracy of an eddy current speed sensor can be neglected for a change of up to 50 % in the gap between coils and the rotating part.

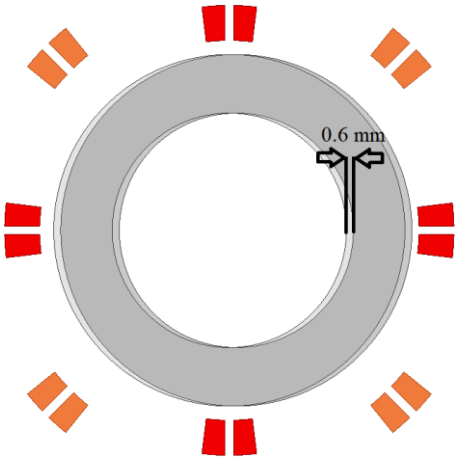

Fig. 21. The model of eccentricity in the eddy current speed sensor

A speed step from 1500 rpm to 3000 rpm with a time rise 0.125 ms is applied, as shown in Fig. 22 a). The voltage to current ratio is calculated using 2D FEM in Fig. 22 b) for a hollow shaft with an aluminum shell. It shows steady state results after only 1 ms; therefore, speed measurement with a high acceleration rate can be achieved using the proposed speed sensor. High excitation frequencies are preferred for a high acceleration rate.

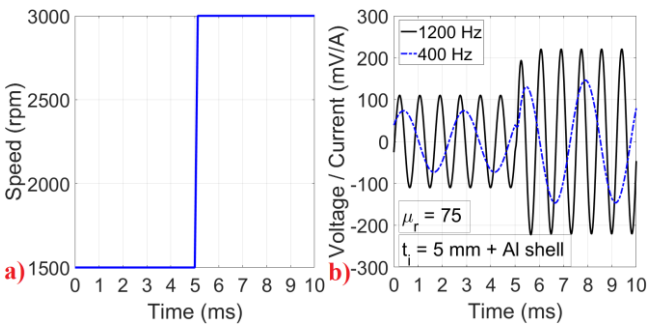

Fig. 22. 2D FEM calculations – solid iron hollow shaft, thickness t_i = 5 mm with aluminum shell, a) speed step, b) the voltage-to-current ratio versus time

Final version of this paper was published at
Measurement 221, 113547, 2023 https://doi.org/10.1016/j.measurement.2023.113547

VIII. Discussions

The performance of the sensor was measured with an aluminum shell and also evaluated using different materials, copper, aluminum, brass, and nonmagnetic stainless steel. A nonmagnetic shell installed on the hollow shaft significantly enhances the sensor output voltage. It was shown that using a thinner shell is achievable. It is critical for the speed sensors in very high speed operation with high excitation frequencies.

The shorter length of the proposed eddy current speed sensor in comparison with the presented sensors in [16] and [34]-[35] helps to accommodate the sensor in compact machines with limited axial space. For example, high power density traction induction machines with shaft oil cooling in Fig. 23 have limited available room in the end regions. Increasing the number of coils helps to decrease the axial length of the sensor while maintaining high sensitivity. Increasing the number of coils to 4 generates a 4-pole machine as shown in Fig. 2 and Fig. 18 in comparison with 2-pole structure sensors in [16] and [35]. The advantages of the rotational eddy current speed sensor with a higher number of poles, similar to the electrical machines, are: 1- shorter end coils, 2- less flux per pole and coil, 3- shorter axial length for nonmagnetic shell. Less flux per pole causes less flux distribution in the air region beyond the coils. It helps to design a more compact magnetic shield in the radial direction to protect the speed sensor against external magnetic and conductive objects and magnetic fields.

The proposed eddy current speed sensor in this paper has four pickup coils in comparison with two pickup coils in [16] and [35]. The induced voltage in each pickup coil is the same. Therefore, each pickup coil can be electrically and physically isolated and separately used for voltage reading. This helps the sensor have a higher electrical fault tolerance capability in the pickup coils in comparison with the two pickup coils sensors in [16] and [35]. This is critical for traction applications with a high probability of overheating and mechanical vibrations, which may cause electrical faults.

The temperature of the shaft affects the properties of the solid shaft, the shell and thus the sensor performance. The conductivity and relative magnetic permeability of solid iron shafts and the conductivity of nonmagnetic shells change with temperature [40]. Fig. 6 and Fig. 7 present the sensor voltage versus conductivity and relative magnetic permeability of solid iron hollow shafts. Using a nonmagnetic shell minimizes electrical properties of the solid iron hollow shaft on the sensor voltage, as shown in Fig. 6 and Fig. 7. The effect of shell conductivity on the sensor voltage is shown in Fig. 20. The advantage of the direct oil cooling of the rotor using a hollow shaft is that the oil inlet temperature in Fig. 23 is controllable and known. This helps to detect shaft temperature for direct recalibration of the eddy current speed sensor for shaft temperature. Eddy current nondestructive evaluation methods could also be used for shaft temperature compensation. The electrical properties of a solid iron hollow shaft and a nonmagnetic conductive shell can be estimated using the eddy current testing method [41]-[44] from measured inductances of the excitation and pickup coils.

The required accuracy for the rotating speed measurement of the rotating machines depends on the traction system. The traction system could be direct drive in-wheel or indirect drive with a gearbox. An accuracy of around 0.4 m/s is approximately considered when using wheel encoders [45]. Therefore, an accuracy of 5-10 rpm is required for in-wheel low speed electrical machines with a maximum speed 1500 rpm. It can be mentioned that the accuracy of 67-133 rpm is calculated for indirect high speed electrical machines with a maximum speed of 20000 rpm. Therefore, the proposed eddy current speed sensor with 0.25 rpm resolution is suitable for electrical and hybrid vehicle applications.

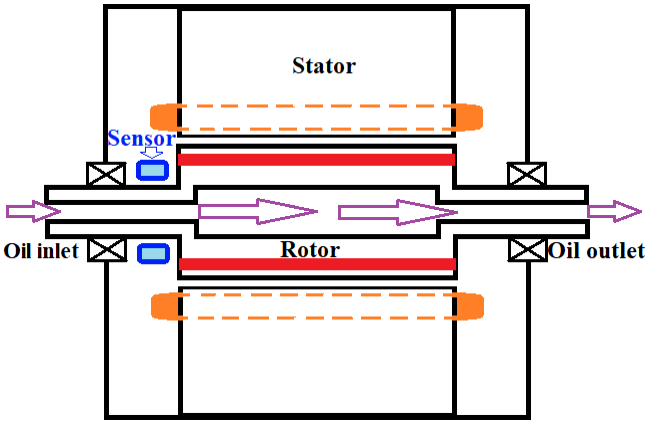

Fig. 23. The schematic model of eddy current speed sensor installed on the hollow shaft in the end region of an electrical machine

IX. Conclusion

An optimum design of an eddy current speed sensor with a short axial length and high sensitivity has been presented. The performance of the sensor has been evaluated in different speed ranges. The calculated nonlinearity errors are always below 1%, with a minimum value of 0.08%.

An aluminum shell provides excellent sensitivity enhancement and minimizes the susceptibility of the sensor to the material properties and the thickness of a hollow iron shaft at higher frequencies.

The presented speed sensor has a simple, contactless and robust structure. The sensor is suitable for rotational speed measurements in different speed ranges, which is critical for traction induction machines in the electro-mobility industry.

Acknowledgment

We thank Dr. Vaclav Grim for his support in performing measurements and in manufacturing the experimental setup.

References

[1] Z. Zhu, et al, “A review of the application of deep learning in intelligent fault diagnosis of rotating machinery,” *Measurement*, vol. 206, 112346, 2023

[2] X. Ma, et al., “A hybrid prognostic method for rotating machinery under time-varying operating conditions by fusing direct and indirect degradation characteristics,” *Measurement*, vol. 2014, 112831, 2023

[3] J. R. Perez-Cardona, J. W. Sutherland, and S. D. Sudhoff, “Optimization-based design model for electric traction motors considering the supply risk of critical materials,” *IEEE Open Access Journal of Power and Energy*, vol. 10, 2023

Final version of this paper was published at
Measurement 221, 113547, 2023 https://doi.org/10.1016/j.measurement.2023.113547

[4] F. Nishanth, J. Van Verdeghem, E. L. Severson, "A review of axial flux permanent magnet machine technology," *IEEE Trans. Ind. Appl*., 2023 (Early access)
[5] Z. Xu, Y. Xu, Y. Gai and W. Liu, "Thermal management of drive motor for transportation: analysis methods, key factors in thermal analysis, and cooling methods - a review," *IEEE Trans. Transport. Elect*., 2023 (Early access)
[6] B. Raghuraman, S. Nategh, A. Boglietti, T. Thiringer, and K. Bergsro, "Design and optimization of induction machines for E-mobility applications," *2022 International Conference on Electrical Machines (ICEM)*, Valencia, Spain, pp. 2142-2148 , 05-08 September 2022
[7] G. Venturini, M. Carbonieri, L. Di Leonardo, and M. Popescu, "Hairpin windings for traction machines: analysis and comparison," *2022 International Conference on Electrical Machines (ICEM)*, pp. 1655-1661, Valencia, Spain, 05-08 September 2022
[8] M. Popescu, L. Di Leonardo, G. Fabri, G. Volpe, N. Riviere, and M. Villani, "Design of induction motors with flat wires and copper rotor for E-vehicles traction system," *IEEE Trans. Ind. Appl*., 2023 (Early access)
[9] B. Dianati, S. Kahourzade, and A. Mahmoudi, "Optimization of axial-flux induction motors for the application of electric vehicles considering driving cycles," *IEEE Trans. Energy Conversion*, vol. 2020, vol. 35, no. 3, pp. 1522 - 1533, 2020
[10] J. Mei, C. H. T. Lee, and J. L. Kirtley, "Design of axial flux induction motor with reduced back iron for electric vehicles," *IEEE Trans. Veh.Tech*., vol. 69, no. 1, pp. 293 - 301, 2020
[11]B. Assaad, K. Mikati, T.V. Tran, and E. Negre, "Experimental study of oil cooled induction motor for hybrid and electric vehicles," *2018 XIII International Conference on Electrical Machines (ICEM)*, pp. 1195-1200, Alexandroupoli, Greece, 03-06 September 2018
[12]R. Wang, X. Fan, D. Li, R. Qu, Z. Liu, and L. Li, "Comparison of heat transfer characteristics of the hollow-shaft oil cooling system for high-speed permanent magnet synchronous machines," *IEEE Trans. Ind. Appl.*, vol. 58, no. 5, pp. 6081-6092, Sept./Oct. 2022
[13]G. Zhu, L. Li, Y. Mei, T. Liu, and M. Xue, "Design and analysis of a self-circulated oil cooling system enclosed in hollow shafts for axial-flux PMSMs," *IEEE Trans. Veh. Tech.*, vol. 71, no. 5, pp. 4879-4888, May 2022
[14]J. Nonneman, I. Evans, S. Vanhee, I. T'Jollyn, and M. De Paepe, "Experimental investigation of a novel direct rotor cooling method for an interior permanent magnet synchronous machine," *2022 28th International Workshop on Thermal Investigations of ICs and Systems (THERMINIC)*, Dublin, Ireland, pp. 1-5, 28-30 September 2022
[15]H. Wang, X. Liu, M. Kang, L. Guo, and Xinmin Li, "Oil injection cooling design for the IPMSM applied in electric vehicles," *IEEE Trans. Transport. Electrif.*, vol. 8, no. 3, pp. 3427-3440, Sept. 2022
[16]M. Mirzaei and V. Grim, "Speed measurement of rotating hollow shafts using an eddy current sensor," *IEEE/ASME Trans. Mechatronics*, vol. 28, no. 1, pp.568-578, 2023
[17] T. Ameid, A. Menacer, H. Talhaoui, and I. Harzelli, "Rotor resistance estimation using Extended Kalman filter and spectral analysis for rotor bar fault diagnosis of sensorless vector control induction motor," *Measurement*, vol. 111, pp. 243-259, 2017
[18] Z. Zhang, G. Wang, Z. Wang, Q. Liu, and Kang Wang, "Neural network based Q-MRAS method for speed estimation of linear induction motor," *Measurement*, vol. 205, 112203, 2022
[19]X. Zhao, et al., "A reliable adaptive estimation method for the installation error of optical angular encoder in outfield tests," *Measurement*, vol. 174, 109035, 2021
[20] M. Dalboni and A. Soldati, "Absolute two-tracked optical rotary encoders based on Vernier method," *IEEE Trans. Instr. & Meas*., vol. 72, 9501412, 2023
[21]F. Zare, Z. Nasiri-Gheidari, F. Tootoonchian, "The effect of winding arrangements on measurement accuracy of sinusoidal rotor resolver under fault conditions," *Measurement*, vol. 131, pp. 162-172, 2019
[22]S. Han and S. Han, "Resolver angle estimation using parameter and state estimation," *Measurement*, vol. 93, pp. 460-464, 2016
[23] J. Hu, J. Zou, F. Xu, Y. Li, and Y. Fu, "An improved PMSM rotor position sensor based on linear Hall sensors," *IEEE Trans. Magnetics*, vol. 48, no. 11, pp. 3591-3594, Nov. 2012
[24]S.-T. Wu, J.-Y. Chen, and S.-H. Wu, "A rotary encoder with an eccentrically mounted ring magnet," *IEEE Trans. Instrumentation & Measurement*, vol. 63, no. 8, pp. 1907-1915, Aug. 2014
[25] C. Gong, A. Tuysuz, M. Flankl, T. Stolz, J. W. Kolar, T. Habetler, "Experimental analysis and optimization of a contactless eddy-current-based speed sensor for smooth conductive surfaces," *IEEE Trans. Ind. Electronics*, vol. 67, no. 10, pp. 8817-8828, Oct. 2020
[26]C. Gong, S. Li, T. Habetler, J. A. Restrepo, and B. Soderholm, "Direct position control for ultrahigh-speed switched-reluctance machines based on low-cost nonintrusive reflective sensors," *IEEE Trans. Ind. Appl*., vol. 55, no. 1, pp. 480-489, Jan.-Feb. 2019.
[27] C. Gong, and T. Habetler, "Design and experimental analysis of an ultra-high speed switched reluctance machine with aerostatic bearings," *IEEE Trans. Transport. Electrification*, vol. 9, no. 2, pp. 2255-2266, June 2023
[28] Y. Wang, W. Hua, C. Zhang, Z. Wu, and H. Zhang, "Concept and implementation of embedded magnetic encoder in flux-switching permanent-magnet machines," *IEEE Trans. Ind. Electronics*, vol. 69, no. 11, pp. 11796-11806, Nov. 2022
[29] C. Zhang, Y. Wang, H. Zhang, Z. Wu, J. Tao, and W. Hua, "Armature reaction on implementation of embedded magnetic encoder in fractional-slot concentrated-winding permanent magnet machines," *IEEE Trans. Ind. Electronics*, vol. 70, no. 7, pp. 6699-6710, July 2023
[30] X. Guo, Y. Wang, X. Chen, Z. Chen, W. Hua, and R. Zhong, "An embedded magnetic encoder based rotor position estimation for switched reluctance machine," *IEEE Trans. Transport. Electrification*, 2023 (Early Access)
[31]G. Tytko, "Measurement of multilayered conductive discs using eddy current method," *Measurement*, vol. 204, 112053, 2022
[32]P. Xu, Y. Chen, L. Liu, and B. Liu, "Study on high-speed rail defect detection methods based on ECT, MFL testing and ACFM," *Measurement*, vol. 206, 112213, 2023
[33]M. Mirzaei, P. Ripka, V. Grim, L. Jelinek, and J. Svatos, "Thickness evaluation of hollow nonmagnetic cylinders utilizing a motional eddy current," *Measurement*, vol. 189, 110463, 2022
[34]M. Mirzaei, P. Ripka, V. Grim, and A. Chirtsov, "Design and optimization of an eddy current speed sensor for rotating rods," *IEEE Sensors J*., vol. 20, no. 2, pp. 12241-12251, 2020
[35] M. Mirzaei, P. Ripka, and V. Grim, "A novel structure of an eddy current sensor for speed measurement of rotating shafts," *IEEE Trans. Energy Conversion*, vol. 38, no. 1, pp. 170 - 179, 2023
[36]K. R. Davey, "Analytic analysis of single- and three-phase induction motors," *IEEE Trans. Magnetics*, vol. 34, no. 5, pp. 3721 - 3727, 1998
[37] J. Gieras, G. E. Dawson, and A. R. Eastham, "Performance calculation for single-sided linear induction motors with a double-layer reaction rail under constant current excitation," *IEEE Trans. Magnetics*, vol. 22, no. 1, pp. 54-62, Jan. 1986
[38] C. Zhang, Z. Li, J. Chen, F. Qiu, and S. Na, "Design and research of a novel non-contact vertical inductive torque sensor," *Measurement*, vol. 1977, 109252, 2021
[39] W. Li, J. Hu, Z. Su, and D. Wang, "Analysis and design of axial inductive displacement sensor," *Measurement*, vol. 187, 110159, 2022
[40] M. Mirzaei, P. Ripka, A. Chirtsov, and V. Grim, "Temperature stability of the transformer position transducer for pneumatic cylinder," *J. Magnetism and Magnetic Materials*, vol. 503, 166636, 1 June 2020
[41] P. Huang, J. Zhao, J. Li, Y. Ding, L. Xu, and Y. Xie, "Conductivity measurement of solid metal rods using high-frequency eddy current method," *IEEE Trans. Instrumentation & Measurement*, vol. 72, 6003111, 2023
[42] P. Huang, et al., "Decoupling conductivity and permeability using sweep-frequency eddy current method," *IEEE Trans. Instrumentation & Measurement*, vol. 72, 6001911, 2023
[43] Z. Xia, et al., "Fast estimation of metallic pipe properties using simplified analytical solution in eddy-current testing," *IEEE Trans. Instrumentation & Measurement*, vol. 72, 1000513, 2023
[44] X. Chen and X. Liu, "Pulsed eddy current-based method for electromagnetic parameters of ferromagnetic materials," *IEEE Sensors J.*, vol. 21, no. 5, pp. 6376-6383, March 2021
[45]E. Klinefelter, and J. A. Nanzer, "Automotive velocity sensing using millimeter-wave interferometric radar," *IEEE Trans. Microwave Theory & Techniques*, vol. 69, no. 1, pp. 1096-1104, Jan. 2021